

Cite this: *Dalton Trans.*, 2020, **49**, 14258

Bistable spin-crossover in a new series of [Fe(BPP-R)₂]²⁺ (BPP = 2,6-bis(pyrazol-1-yl)pyridine; R = CN) complexes†

Kuppasamy Senthil Kumar,  *‡^{a,b} Nicolas Del Giudice,  ^a Benoît Heinrich,  ^a Laurent Douce  ^a and Mario Ruben  *^{a,b,c}

Spin-crossover (SCO) active transition metal complexes are a class of switchable molecular materials. Such complexes undergo hysteretic high-spin (HS) to low-spin (LS) transition, and *vice versa*, rendering them suitable for the development of molecule-based switching and memory elements. Therefore, the search for SCO complexes undergoing abrupt and hysteretic SCO, that is, bistable SCO, is actively carried out by the molecular magnetism community. In this study, we report the bistable SCO characteristics associated with a new series of iron(II) complexes—[Fe(BPP-CN)₂](X)₂, X = BF₄ (**1a–d**) or ClO₄ (**2**)—belonging to the [Fe(BPP-R)₂]²⁺ (BPP = 2,6-bis(pyrazol-1-yl)pyridine) family of complexes. Among the complexes, the lattice solvent-free complex **2** showed a stable and complete SCO (*T*_{1/2} = 241 K) with a thermal hysteresis width (ΔT) of 28 K—the widest ΔT reported so far for a [Fe(BPP-R)₂](X)₂ family of complexes, showing abrupt SCO. The reproducible and bistable SCO shown by the relatively simple [Fe(BPP-CN)₂](X)₂ series of molecular complexes is encouraging to pursue [Fe(BPP-R)₂]²⁺ systems for the realization of technologically relevant SCO complexes.

Received 22nd June 2020,
Accepted 11th September 2020

DOI: 10.1039/d0dt02214d

rsc.li/dalton

Introduction

The captivating phenomenon of spin-crossover (SCO)^{1–10} exhibited by molecular systems composed of first-row transition metal ions—featuring d⁴–d⁷ electronic configurations—is of significance in chemistry,^{11–21} materials science,^{16,21–26} biology,²⁷ and geology.²⁸ In chemistry and materials science, the synthesis and structure–property relationship studies of SCO active molecular complexes are actively pursued to

develop molecule-based switching and memory architectures.^{24,29} Molecular complexes featuring abrupt and hysteretic spin-state switching, that is, bistable SCO, are especially suited for switching and memory applications.^{30–33} Iron(II) complexes composed of all nitrogen-based BPP (BPP = 2,6-bis(pyrazol-1-yl)pyridine) ligand systems are a prominent example of SCO complexes exhibiting bistable SCO.^{34–39} Various parameters, for example, intermolecular interactions, molecular packing, and electronic substituent effects, governing the occurrence and nature of SCO—gradual, abrupt, and bistable—in [Fe(BPP-R)]²⁺ complexes have been elucidated.¹³ Although some [Fe(BPP-R)]²⁺ complexes show bistable SCO, the thermal hysteresis width (ΔT) associated with the spin-state switching of the complexes is well below the value of $\Delta T \geq 40$ K, desirable for technological applications.²²

A systematic molecular-engineering-based approach and a clear elucidation of factors governing SCO are the need of the hour to obtain [Fe(BPP-R)]²⁺ complexes featuring wide ΔT .⁴⁰ Although there is some understanding on the structural features governing SCO in the [Fe(BPP-R)]²⁺ complexes, a pre-synthesis design of [Fe(BPP-R)]²⁺ complexes capable of showing $\Delta T \geq 40$ K is still marred by the complex interplay between the SCO event and various structural parameters governing the spin-state switching. Therefore, the realization of technologically useful [Fe(BPP-R)]²⁺ complexes could only be achieved by systematically varying the R group on [Fe(BPP-R)]²⁺ complexes

^aInstitut de Physique et Chimie des Matériaux de Strasbourg (IPCMS), CNRS-Université de Strasbourg, 23, rue du Loess, BP 43, 67034 Strasbourg cedex 2, France. E-mail: kavinsenthil82@gmail.com

^bInstitute of Nanotechnology (INT), Karlsruhe Institute of Technology (KIT), Hermann-von-Helmholtz-Platz 1, 76344 Eggenstein-Leopoldshafen, Germany. E-mail: mario.ruben@kit.edu

^cInstitute of Quantum Materials and Technologies (IQMT), Karlsruhe Institute of Technology (KIT), Hermann-von-Helmholtz-Platz 1, 76344 Eggenstein-Leopoldshafen, Germany

† Electronic supplementary information (ESI) available: X-ray crystal structure of **2-cryst**, electronic absorption spectra of the ligand and complexes; χ_{MT} versus *T* and $d(\chi_{MT})/dT$ versus *T* plots of complexes **1b**, **1c**, and **1d**; differential scanning calorimetric (DSC) analyses of complexes **1c** and **1d**. CCDC 1961768 and 2010806. For ESI and crystallographic data in CIF or other electronic format see DOI: 10.1039/D0DT02214D

‡ KSK dedicates this article to Sarvaseva School, Kollanvalasu, Erode, Tamil Nadu, India, and his elementary school teachers for their support, guidance, and selfless dedication, empowering underprivileged children.

on an experimental basis. The recently reported [Fe(BPP-COOEt)₂](ClO₄)₂·CH₃CN complex is a prominent example of such an effort. The complex has shown a thermal hysteresis width of 101 K ($T_{1/2} = 233$ K) for the first HS → LS → HS cycle—the highest ΔT reported so far for an [Fe(BPP-R)]²⁺ complex; however, the SCO of the complex was not stable in the subsequent cycles.⁴¹ This shortcoming prompted us to search for a new series of [Fe(BPP-R)]²⁺ complexes that could exhibit stable and bistable SCO characteristics. Consequently, we have designed and synthesized a new ligand—2,6-bis(1*H*-pyrazol-1-yl)pyridine-4-carbonitrile (BPP-CN)—featuring a CN substituent at the 4-position of the central pyridine ring of the BPP skeleton. In this study, we report the bistable SCO characteristics of a [Fe(BPP-CN)₂](X)₂, X = BF₄ (**1a–d**) or ClO₄ (**2**) series of complexes.

Results and discussion

The BPP-CN ligand (**L**) was synthesized from the precursor 4-iodo-2,6-bis(1*H*-pyrazol-1-yl)pyridine (I-BPP) by performing the classical Rosenmund–von Braun reaction⁴² as shown in Chart 1.

Addition of solid [Fe(BF₄)₂]₂·6H₂O to a clear acetonitrile (ACN) solution of the ligand followed by gentle swirling resulted in the formation of a homogeneous solution, which was allowed to stand undisturbed for a week. This procedure resulted in the formation of an orange microcrystalline form of [Fe(BPP-CN)₂](BF₄)₂—**1a**—at the bottom of the reaction vial.

Slow diffusion of diethyl ether (Et₂O) into the orange filtrate, obtained after the separation of **1a**, yielded orange plate-like (**1b**) and red rod-like (**1c**·ACN, referred to as **1c** for clarity) crystalline forms of [Fe(BPP-CN)₂](BF₄)₂; complexes **1b** and **1c** were manually separated for further analyses. X-ray diffraction studies of the red rod-like crystals confirmed the formation of the expected iron(II) complex, as shown in Chart 1. On the other hand, the attempted structure determination of the orange plate-like crystals was not fruitful due to the bad quality of the crystals. To analyse the role of crystallinity on the SCO characteristics, the powder form of [Fe(BPP-CN)₂](BF₄)₂—**1d**—was prepared using a 1:1 acetonitrile/dichloromethane solvent mixture.

Remarkably, rapid precipitation of complex **2** occurred after the addition of solid [Fe(ClO₄)₂]₂·6H₂O to a clear ACN solution of **L**; the complex was collected by filtration after stirring the heterogeneous reaction mixture for two hours under ambient conditions. Attempts to crystallise the complex from the filtrate by diffusing Et₂O into the filtrate were not successful. On the other hand, storage of the mother liquor in a fridge at 4 °C for three months yielded a few crystals of the complex, referred to as **2-cryst**, suitable for X-ray structural analysis, see the discussion below.

Complex **1c** crystallised with a lattice ACN solvent molecule (Fig. 1a) in the chiral *P*₂₁₂₁₂ space group, belonging to the orthorhombic crystal system. The average bond lengths and angular parameters (Table 1 and Chart S1†) indicate the LS-state of the complex at 293 K. Short contacts between ACN/ClO₄[−] and [Fe(BPP-CN)₂]²⁺ entities guided the molecular

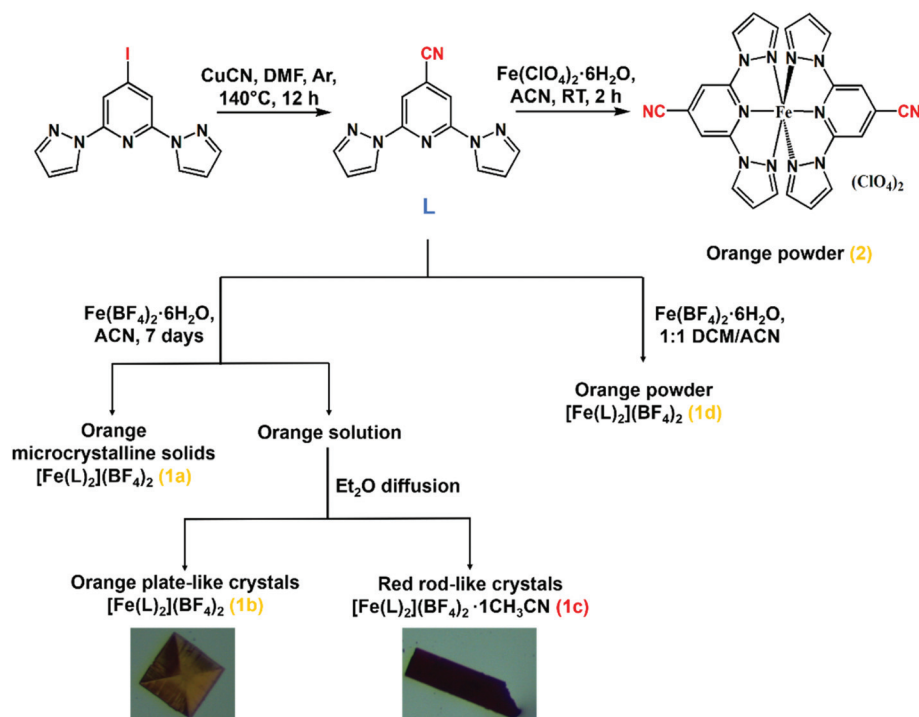


Chart 1 Synthetic step involved in the preparation of **L**, and the methodology devised to prepare complexes **1a–d** and complex **2**.

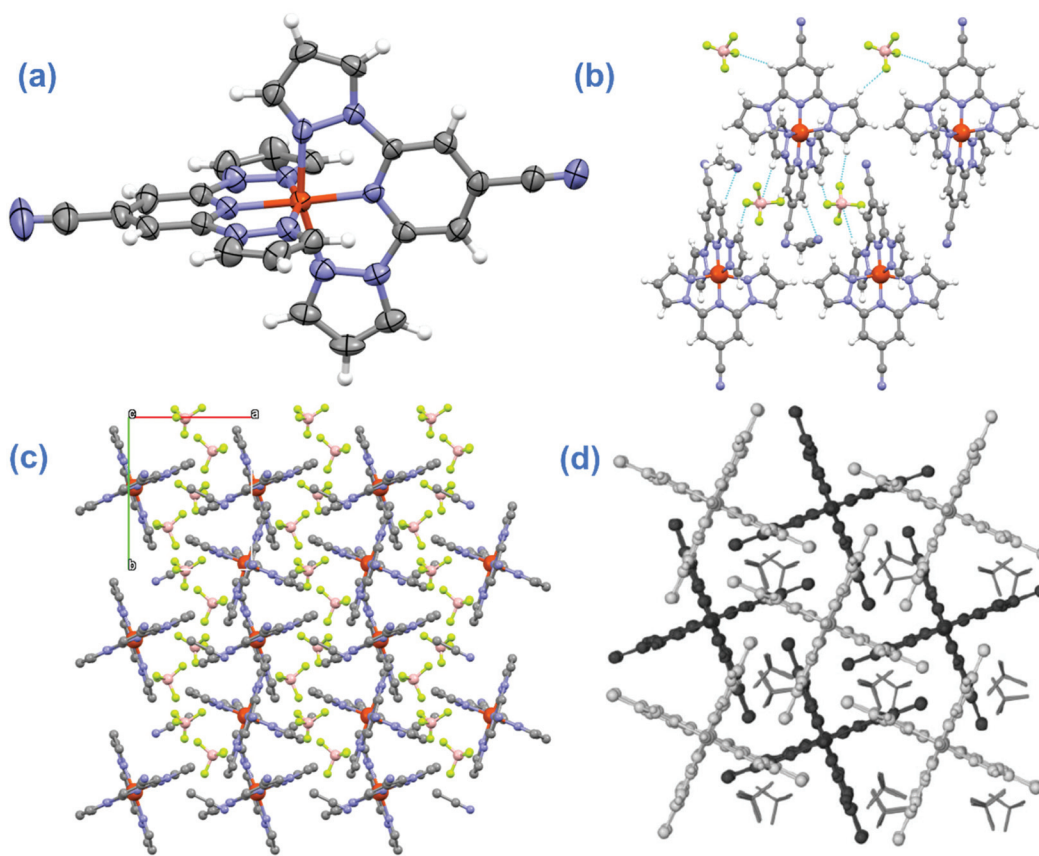


Fig. 1 (a) X-ray structure of complex **1c** (CCDC 1961768). Lattice ACN solvent and counter anions are omitted for clarity, (b) intermolecular short contacts observed in the crystal lattice of **1c**, (c) non-terpyridine-embrace lattice packing pattern observed for complex **1c** in the crystal lattice, and (d) typical terpyridine embrace lattice packing pattern observed for the $[\text{Fe}(\text{1-BPP-R})_2](\text{X})_2$ family of complexes; image reproduced with permission from ref. 43, copyright Royal Society of Chemistry 2007.

Table 1 Average Fe–N bond lengths (Å), angles ($^\circ$), and distortion indices ($^\circ$) of complexes **1c** and **2-cryst** (CCDC 2010806). ϕ is the *trans*-N{pyridine}–Fe–N{pyridine} angle; ψ is the N{pyrazole}–Fe–N{pyrazole} clamp angle; Σ is the distortion index, calculated using the relation $\sum_{i=1}^4 = |90 - i|$, where i is one of the twelve *cis*-N–Fe–N angles; θ is the angle between the planes of the two ligands; α is the average value of four *cis*-N{pyridyl}–Fe–N{pyrazole} angles. The angles ϕ and θ represent the degree of distortion; complexes with ideal octahedral geometry have $\phi = 180^\circ$ and $\theta = 90^\circ$

Parameter	Value	
	1c	2-cryst
T/K	293	293
rFe–N (average)	1.9(4)	1.9(3)
$\text{N}_3\text{–Fe}_1\text{–N}_9$ (ϕ)	176.9(3)	176.5(2)
$\text{N}_7\text{–Fe}_1\text{–N}_x$ (ψ)	160.4(3)	160.8(9)
$\text{N}_1\text{–Fe}_1\text{–N}_x$ (ψ)	161.1(3)	160.6(2)
Σ	84.0(6)	83.1(7)
θ	85.4(4)	87.7(8)
α	80.4(0)	80.4(1)

^a $x = 12$ (**1c**) and 11 (**2-cryst**). ^b $x = 4$ (**1c**) and 5 (**2-cryst**).

organization in the crystal lattice (Fig. 1b). Remarkably, the $[\text{Fe}(\text{BPP-CN})_2]^{2+}$ units packed in a non-terpyridine-embrace mode (Fig. 1c). Such packing is a deviation from the terpyridine-embrace lattice packing mode (Fig. 1d)^{13,43} observed for the $[\text{Fe}(\text{BPP-R})]^{2+}$ family of complexes exhibiting bistable SCO (*vide infra*).

Lattice solvent-free **2-cryst** crystallized in the $P21/a$ space group, belonging to the monoclinic crystal system (Fig. S1a†). The average of the N–Fe–N bond lengths and angular components (Table 1) of **2-cryst** indicate the LS-state of the complex at RT. Intermolecular short contacts between the lattice anions and the complex cations guided the non-terpyridine embrace packing pattern in the crystal lattice, as shown in Fig. S1b and c.† In stark contrast to the LS-state of **2-cryst**, a HS-state was observed for **2** at 293 K (*vide infra*). A comparison between the powder X-ray diffraction pattern of **2** and simulated X-ray pattern of **2-cryst**, obtained from the single crystal studies, revealed different molecular organizations in the powder and crystalline forms of the complexes (Fig. S2†). Such differing molecular organizations in the crystallographically different phases of **2** and **2-cryst** rendered the complexes HS and LS, respectively, at 293 K. No further analyses and mag-

netic studies of **2-cryst** were performed due to the small quantity of the crystals obtained from the crystallization process. Hence, the structural description of **2-cryst** only serves the purpose of elucidating the expected complex formation.

Electronic absorption spectra of **L**, **1a**, and **2** measured in acetonitrile showed absorption maxima (Fig. S3 and Table S1†) in the UV region, corresponding to the electronic transitions originating from the ligand skeleton. The absence of a metal-to-ligand charge transfer ¹(MLCT) feature in the visible region indicates the HS-state of the complexes in the solution.

All complexes reported in this study are SCO active, as inferred from the variable temperature magnetic measurements. Complexes **1a**, **1b**, **1d**, and **2** showed reproducible, abrupt, and hysteretic SCO, whereas complex **1c** showed a lattice solvent dependent SCO that varied with the cycle. Remarkably, a reversible and reproducible bistable SCO was observed for **1c** after *in situ* solvent removal of the complex inside a SQUID-VSM (MPMS 3) magnetometer at 400 K. Complexes **1d**, solvent-free **1c**, and **2** showed one-step SCO, facilitating the straightforward estimation of ΔT from the peak positions of $d(\chi_M T)/dT$ (first derivative) *versus* T plots. In contrast, shoulder-like features were observed in the heating (LS \rightarrow HS) branches of the $\chi_M T$ *versus* T plots of **1a–c**, making the estimation of ΔT less straightforward. To address this issue, critical transition temperatures associated with the cooling ($T_{c\downarrow}$) and heating ($T_{c\uparrow}$) branches of $\chi_M T$ *versus* T plots were obtained from the peak positions of $d(\chi_M T)/dT$ *versus* T plots; hysteresis widths were calculated using the relation $\Delta T = (T_{c\uparrow} - T_{c\downarrow})$, as shown in Fig. 2; thus for each of complexes **1a–c**, at least two different ΔT values are reported. The temperature at which a 1 : 1 ratio of HS- and LS-states is observed is reported as $T_{1/2}$ (Fig. 2b).

Complexes **1a** and **1b** showed comparable bistable SCO, as shown in Fig. 2a and S4,† respectively; the SCO remained stable to cycling, except for small differences among the cycles. A notable difference is the occurrence of the HS to LS switching at higher temperatures in the second and subsequent cooling steps relative to the first cooling step.

Unlike the HS to LS switching, which proceeded in a single step, the LS to HS switching of the complexes proceeded in a stepwise manner. A small shoulder-like intermediate region⁴⁴ centred around 241 K, featuring almost equal proportions of HS and LS complexes, was observed for **1a** in the LS to HS switching branch of the first cycle. For complex **1b**, such a shoulder-like region, centred around 253 K, appeared in the first cycle after reaching a composition in which the HS population (82%) is dominant (Fig. S4a†). For both complexes, the onset temperature of shoulder formation and HS fraction increased with increasing the cycle number—the effect is more pronounced for **1a** than for **1b**. The occurrence of shoulder-like features in the first and subsequent heating cycles resulted in the formation of differently sized hysteresis widths for the complexes. In cycle four, ΔT values of 15 K and 4 K were estimated for **1a** above and below the shoulder, respectively (Fig. 2b). Similar values were observed for complex **1b** in the fifth cycle (Fig. S4b†). A $T_{1/2} = \sim 241$ K at $\chi_M T = \sim 1.95$ cm³

mol⁻¹ K was estimated for **1a** and **1b** in cycles four and five, respectively. To analyse the origin of the shoulder formation in the heating branches of **1a** and **1b**, scan rate-dependent magnetic measurements (Fig. S5†) were performed for **1b** by taking the complex as a representative example. Similar $\chi_M T$ *versus* T profiles and comparable $\chi_M T$ values in the shoulder-region were obtained for the scan rates of 0.2 K min⁻¹ (sweep mode) and 10 K min⁻¹ (sweep and settle modes). Such observation rules out the presence of a hidden LS phase or a reverse SCO event contributing to the shoulder formation, as reported for some SCO systems.^{45–47} A crystallographic phase change mediated by the bending of the –CN substituent could have caused the formation of shoulder-like regions in the heating branches of **1a** and **1b**. Such tentative attribution is in line with a literature report detailing the appearance of a shoulder in the cooling branch of an iron(II)-BPP complex—[Fe(BPP-SCH₃)₂](ClO₄)₂—featuring an –SCH₃ substituent at the fourth position of the pyridine ring of the BPP skeleton. A crystallographic phase change, caused by the rotation of almost half of the –SCH₃ substituents, effected the formation of the shoulder in the cooling branch of the $\chi_M T$ *versus* T profile of [Fe(BPP-SCH₃)₂](ClO₄)₂, as inferred from variable-temperature SCXRD studies. The poor crystallinity of complexes **1a** and **1b** prohibited us from performing such variable-temperature SCXRD studies. Thus, the molecular origin of the shoulder formation in the LS \rightarrow HS switching branches of **1a** and **1b** remains to be elucidated unambiguously.

A lattice solvent-dependent SCO is observed for complex **1c**. In all cycles, the spin-state switching took place in an abrupt manner until a particular LS : HS composition is reached, as shown in Fig. S6.† After that, the switching became gradual, resulting in the formation of two different hysteretic regions composed of dominant HS or LS fractions; for example, such regions featuring $\Delta T = 66$ K and 6 K were observed in the second cycle (Fig. S6b†). Remarkably, a plateau-like region bridged the abrupt and gradual regions of the first cycle and the LS to HS switching (heating) branch of the second cycle. In the HS to LS switching branch of the second and subsequent cycles, such plateau-like regions disappeared, and the SCO became steadily gradual after the occurrence of initial abrupt switching. The $T_{1/2}$ steadily decreased at each cycle, starting from the first cycle. A $T_{1/2} = 247$ K was obtained for the fourth heating branch, which is close to the value of $T_{1/2} = 243$ K obtained for the heating branches of complexes **1a** (cycle 4) and **1b** (cycle 5). The comparable nature of the small- and wide-angle X-ray scattering (SWAXS) patterns (Fig. 3) of **1c**—obtained after thermal cycling—and solvent-free **1a** indicates the conversion of the ACN solvated **1c** into a solvent-free phase **1c**, which has a similar molecular organization and SCO characteristic—in the fourth heating branch—as that of **1a**.

Such observation elucidates the gradual loss of the ACN solvent molecule from the crystal lattice of **1c** during the switching process and complete removal of the lattice solvent after the third cycle. The foregoing description illustrates a complicated relationship between the lattice solvent content and SCO property.^{41,48–51}

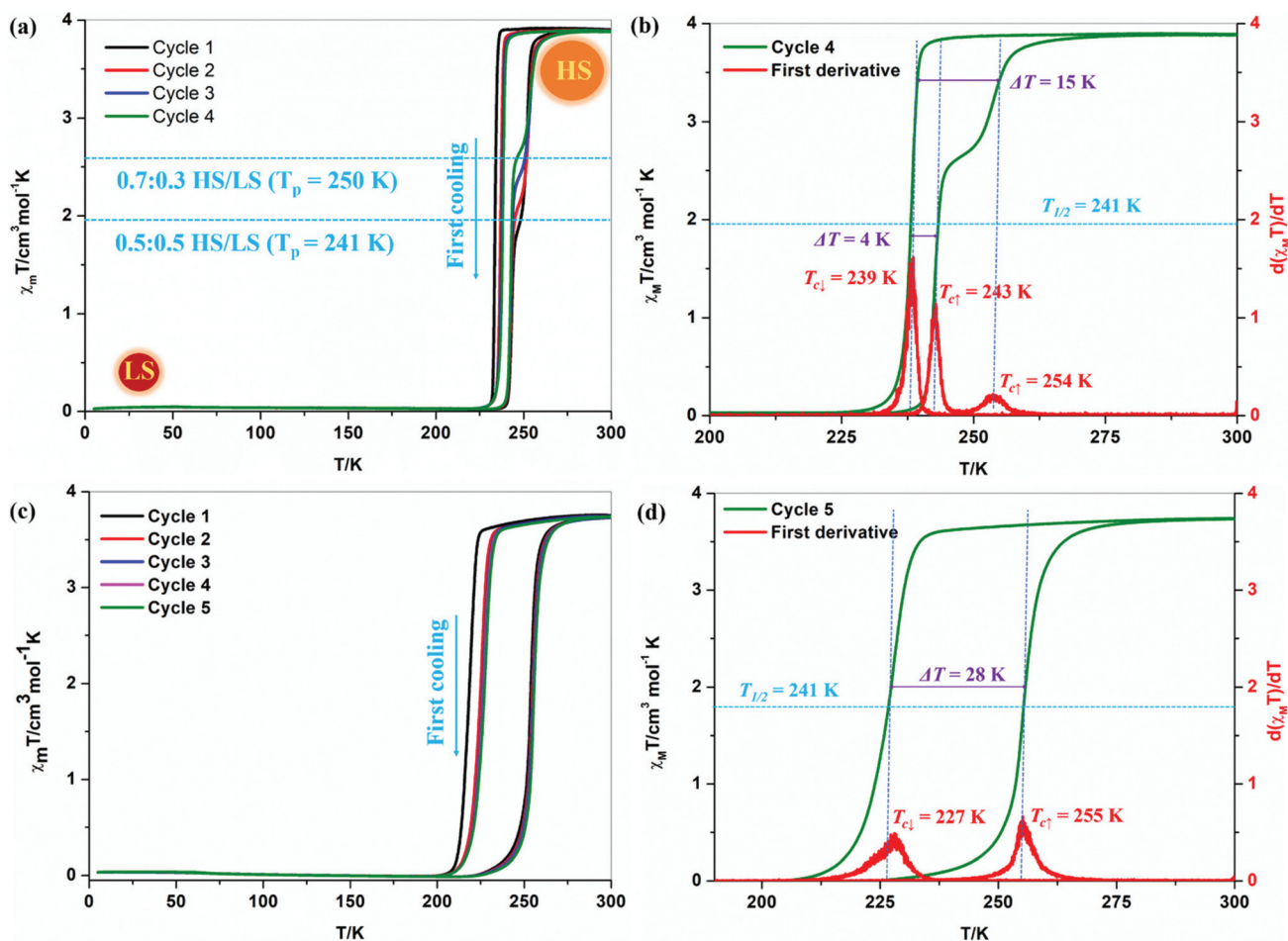


Fig. 2 Bistable SCO characteristics of complexes **1a** and **2**. $\chi_M T$ versus T plots of complex **1a** (a) and **2** (c). $\chi_M T$ versus T and $d(\chi_M T)/dT$ versus T plots of **1a** (b) and **2** (d), corresponding to cycles 4 and 5, respectively. T_p is the temperature at which the centre of the step-like region is situated. The critical temperatures (T_c) associated with the cooling and heating branches are designated as T_{c1} and T_{c1} , respectively. Experiments were performed in settle mode under an applied DC field of 0.1 T; scan rates of 5 K min^{-1} and 1 K min^{-1} were employed for cycles 1–3 and subsequent cycles, respectively.

To elucidate the SCO characteristics of the solvent-free phase of **1c**, experiments were performed by heating a freshly prepared sample of solvated **1c** *in situ* inside the SQUID-VSM magnetometer at 400 K for three hours. Elemental analysis data of **1c** obtained after the magnetic measurements confirm the complete removal of lattice ACN (see Experimental section). The $\chi_M T$ versus T plots (Fig. 4) of the solvent-free phase of **1c** revealed a stable and reproducibly bistable SCO— $T_{1/2} = 241 \text{ K}$ and $\Delta T = 10 \text{ K}$.

The SCO in solvent-free **1c** proceeds with a larger 10 K thermal hysteresis width than the hysteresis widths observed for **1a** and **1b**. Remarkably, the $\Delta T = 10 \text{ K}$ observed for solvent-free **1c** is comparable with the hysteresis widths—11 K (cycle 1) and 8 K (cycles 2–5)—observed for **1d** (see Fig. S7†). The SCO in the cooling branch occurred in a gradual manner until reaching a particular LS : HS composition; after that, an abrupt switching was observed. On the other hand, a partial and abrupt LS \rightarrow HS switching occurred before the onset of the gradual phase in the heating branch. Similar spin-state switch-

ing characteristics were also observed in the DSC curves of solvent-free **1c** (Fig. S8† and Table 2). The split peaks observed in the heating and cooling DSC curves correspond to the mid-point and onset temperatures of the abrupt and gradual spin-state switching events. Our attempts to obtain the X-ray structure of solvent-free **1c** were not successful due to the cracking of the crystals during temperature cycling.

The rapidly precipitated complex **1d** showed an incomplete and hysteretic SCO with the switching temperature centred around 231 K and 233 K for the first and subsequent cycles, respectively (Fig. S7†). At 300 K, a $\chi_M T$ value of 2.5 $\text{cm}^3 \text{mol}^{-1} \text{K}$ was obtained, indicative of a composition made of a dominant HS fraction contaminated with a LS fraction. As in the cases of **1a** and **1b**, the HS to LS switching of the second and subsequent cycles of **1d** occurred at a higher temperature relative to the first cycle. This resulted in the reduction of thermal hysteresis width associated with cycles 2–5 ($\Delta T = 8 \text{ K}$) in comparison with the first cycle ($\Delta T = 11 \text{ K}$).

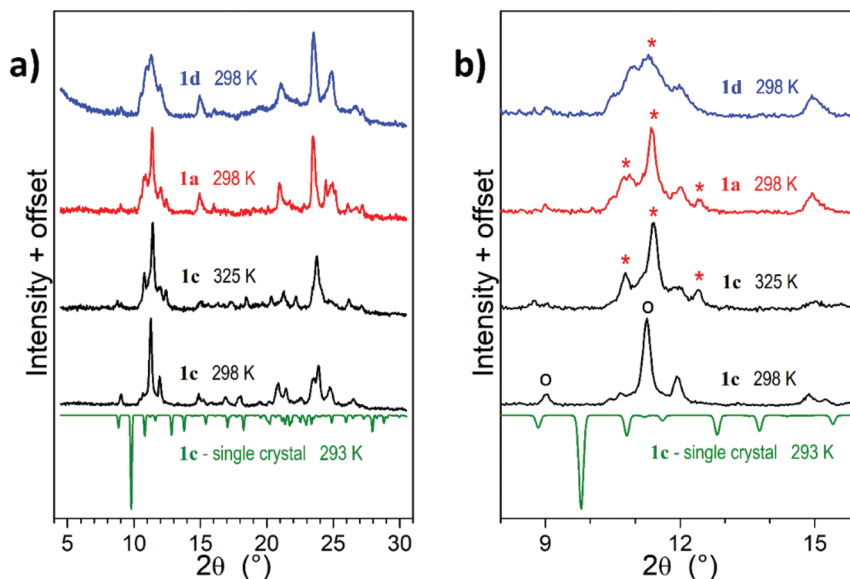


Fig. 3 (a) Small- and wide-angle X-ray scattering (SWAXS) patterns of complexes **1a** (crystallized without a lattice solvent), **1c** (crystallized with a lattice solvent), and **1d** (solvent-free powder), as compared to the pattern simulated from the single-crystal structure of **1c**; (b) expanded portion of (a) in the $2\theta = 8^\circ$ – 16° range; the stars and rings point the relevant reflections for comparison. The **1c** crystals used for SC-XRD and SWAXS analysis display different structures, presumably due to the partial lattice solvent removal during the storage under ambient conditions. After heating, the patterns of **1c** became similar to **1a**, revealing the release of the lattice solvent. The SWAXS patterns of solvent-free structures **1a** and **1d** are also similar; the broadened reflections observed for **1d** are due to the small crystal size.

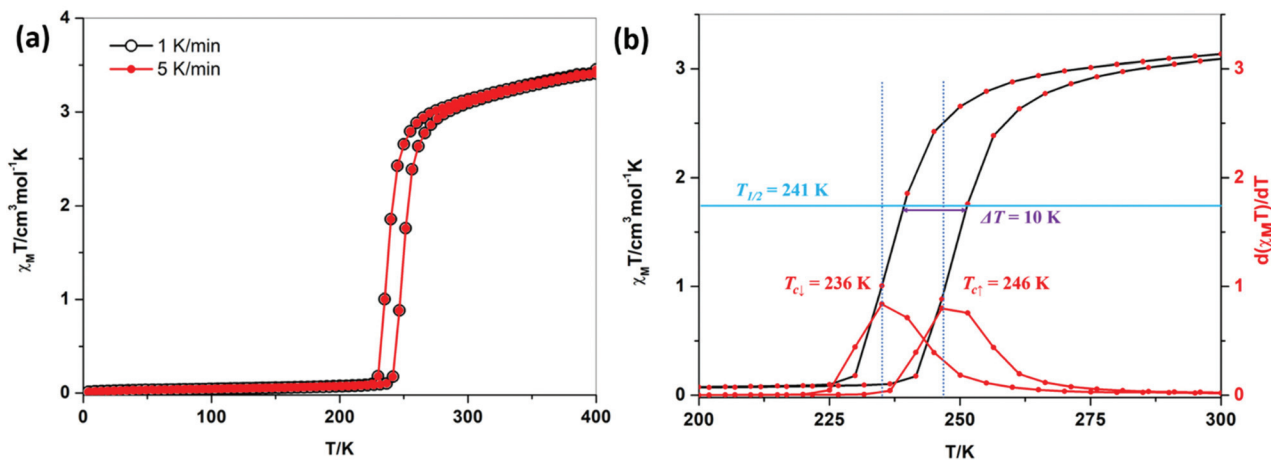


Fig. 4 Bistable SCO characteristic of lattice solvent-free **1c**. (a) $\chi_M T$ versus T plots of solvent-free **1c** at scan rates of 5 K min^{-1} (cycle 1) and 1 K min^{-1} (cycle 2), and (b) $\chi_M T$ versus T plot and the corresponding $d(\chi_M T)/dT$ versus T plot of solvent-free **1c** obtained at 5 K min^{-1} . The critical temperatures (T_c) associated with the cooling and heating branches are designated as T_{c1} and T_{c2} , respectively. Experiments were performed in settle mode under an applied DC field of 0.1 T .

Complex **2**— $[\text{Fe}(\text{L})_2](\text{ClO}_4)_2$ —showed bistable SCO with the widest and stable ΔT among the complexes reported in this study, as shown in Fig. 2c and d; the spin-state switching occurred in a straightforward manner without any intermediate region. In the first cycle, upon cooling from 300 K ($\chi_M T = 3.7 \text{ cm}^3 \text{ mol}^{-1} \text{ K}$), an abrupt HS to LS switching occurred; subsequent heating resulted in the occurrence of LS to HS switching at a higher temperature relative to the HS to LS switching, rendering the SCO hysteretic—a $\Delta T = 35 \text{ K}$ is observed at $T_{1/2} =$

237 K . In the second and subsequent cooling, the abrupt HS to LS switching proceeded at a higher temperature relative to the first HS to LS switching. This resulted in the reduction of thermal hysteresis width and an increase of $T_{1/2}$ for the cycles 2–5 relative to the first cycle— $\Delta T = 28 \text{ K}$ and $T_{1/2} = 241 \text{ K}$ were calculated for the fifth cycle.

Differential scanning calorimetry (DSC) experiments further substantiated the reproducible nature of the SCO in complexes **1a**, solvent-free **1c**, **1d**, and **2**. Since complexes **1a**

Table 2 Parameters associated with the SCO of the complexes discussed in this study

Complex	SQUID		DSC	
	$\chi_M T/cm^3 \text{ mol}^{-1} \text{ K}$ (at 300 K) ^a	$T_{1/2}/\text{K}$ and $\Delta T/\text{K}$ (at $T_{1/2}$) ^b	$T_{1/2}/\text{K}$ and $\Delta T^{\text{c,d}}/\text{K}$	ΔH and $\Delta S^{\text{e,f}}$
1a	3.87	241 and 4 (cycle 4)	240 and 6 (cycle 4)	13.8 and 57.5
1b	3.91	241 and 4 (cycle 5)		
Solvent-free 1c	3.12	241 and 10 (cycle 2)	241 and 10 (cycle 1)	12.75 and 52.93
1d	2.47	233 and 7 (cycle 5)	234 and 8 (cycle 4)	8.15 and 34.83
2	3.75	247 and 28 (cycle 5)	241 and 32 (cycle 4)	12.36 and 51.29

^a For the last performed cycle. ^b Scan rate = 1 K min⁻¹. ^c Scan rate = 2 K min⁻¹. ^d DSC measurements were not performed for **1b**. ^e Calculated using the relation $\Delta S = \Delta H/T_{1/2}$. ^f ΔH in kJ mol⁻¹ and ΔS in J K⁻¹ mol⁻¹.

and **1b** feature similar SCO characteristics, DSC experiments were not performed for complex **1b**. Overall, the $T_{1/2}$ and ΔT values obtained from the DSC measurements, performed at a scan rate of 2 K min⁻¹ (Fig. 5 and S8†), are comparable with the values obtained from magnetic measurements (Table 2).

The DSC experiments were also used to derive the enthalpy (ΔH) and entropy (ΔS) variations associated with the SCO of the complexes. Although valid only for the case of solution-phase SCO, the relation $\Delta S = \Delta H/T_{1/2}$ is often used in the literature to describe the entropy variation associated with spin-state switching in the solid state.⁵² Therefore, to facilitate a meaningful comparison with the literature reported values, we have used the relation $\Delta S = \Delta H/T_{1/2}$ to calculate the entropy values associated with the SCO of the complexes. The experimentally deduced ΔH and ΔS values collected in Table 2 are in the range reported for iron(II)-SCO complexes.^{52,53} As often reported, the entropy values are greater than 13.4 J K⁻¹ mol⁻¹ expected solely on the $S = 0$ to $S = 2$ spin multiplicity change occurring upon SCO: the excess entropy is ascribed to the differing intramolecular vibrational modes coupled with the spin-state switching of the complexes.^{54,55}

The abrupt and hysteretic spin-state switching characteristics shown by the complexes reported in this study are remarkable. In the absence of single-crystal X-ray diffraction studies, it is difficult to ascribe the factors contributing to the occurrence of hysteretic SCO behaviour in complexes **1a–b**, **1d**, and **2**. However, some tentative insights could be drawn from the literature reports describing SCO in the [Fe(BPP-R)₂]²⁺ series of complexes. Although the spin-state switching in [Fe(BPP-R)₂]²⁺ complexes is often reported to proceed with thermal hysteresis widths in the range of 1–4 K, only a handful of [Fe(BPP-R)₂]²⁺ complexes are reported to show SCO with ΔT larger than 4 K. Notable examples are [Fe(BPP-COOEt)₂](ClO₄)₂·1CH₃CN,⁴¹ [Fe(BPP-CH₂Br)₂](BF₄)₂·4MeNO₂,⁵⁶ and [Fe(BPP-CH₃)₂](ClO₄)₂.⁵² Complex [Fe(BPP-COOEt)₂](ClO₄)₂·1CH₃CN showed abrupt and hysteretic SCO with $\Delta T = \sim 101$ K ($T_{1/2} = 233$ K); however, the SCO of the complex is not stable and varied with cycling. Thermal hysteresis widths of 31 K ($T_{1/2} = 340$ K) and 18 K ($T_{1/2} = 184$ K) were reported for [Fe(BPP-CH₂Br)₂](BF₄)₂·4MeNO₂ and [Fe(BPP-CH₃)₂](ClO₄)₂, respectively. While the SCO profile of [Fe(BPP-CH₃)₂](ClO₄)₂ is comparable, except for $T_{1/2}$ and ΔT , with the one observed for complex **2**, the SCO in [Fe(BPP-CH₂Br)₂](BF₄)₂·4MeNO₂ is gradual. Thus, the 28 K thermal hysteresis width reported in this study for

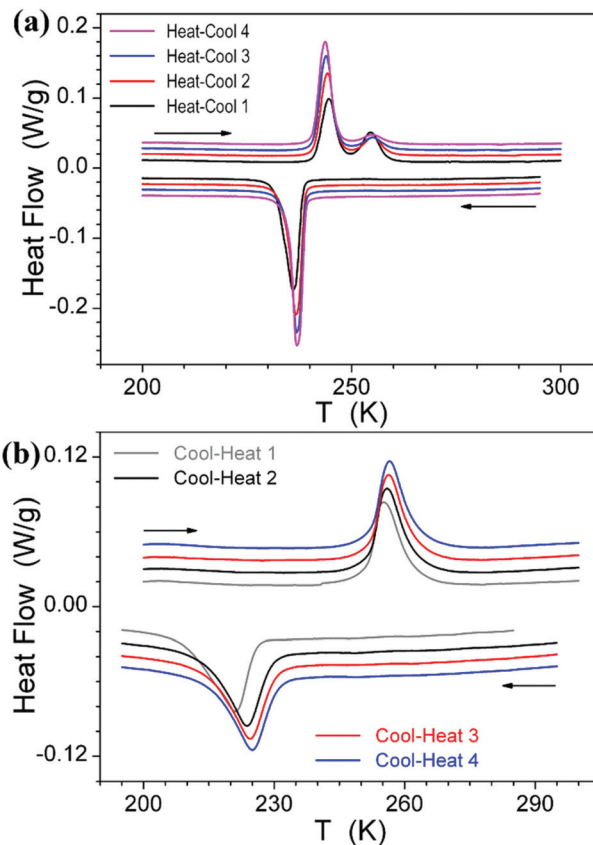


Fig. 5 Differential scanning calorimetry (DSC) curves of complexes (a) **1a** and (b) **2**. A scan rate of 2 K min⁻¹ was employed; endotherm (up). The close correlation between the $\chi_M T$ versus T plots (Fig. 2 and 4) and DSC curves confirms the reproducible nature of the SCO associated with the complexes discussed in this study.

complex **2** is the widest stable ΔT reported so far for an [Fe(BPP-R)₂]²⁺ complex, exhibiting abrupt spin-state switching.

Attempts have been made to establish the relation between bistable SCO and molecular organization in the iron(II)-BPP family of complexes. Thereby, a terpyridine embrace packing pattern⁴³ and Jahn–Teller (J–T) distorted HS-states have been attributed to the occurrence of hysteretic SCO in [Fe(BPP-CH₂Br)₂](BF₄)₂·4MeNO₂ and [Fe(BPP-CH₃)₂](ClO₄)₂. On the other hand, a J–T distorted HS-state and non-terpyridine

embrace packing pattern was observed for $[\text{Fe}(\text{BPP-COOEt})_2](\text{ClO}_4)_2 \cdot 1\text{CH}_3\text{CN}$, which showed $\Delta T = 101$ K. The bistable SCO in complex $[\text{Fe}(\text{BPP-COOEt})_2](\text{ClO}_4)_2 \cdot 1\text{CH}_3\text{CN}$ is thus primarily ascribed to the occurrence of a pronounced J–T distortion in combination with some favourable intermolecular interactions.⁴¹ Specifically, while the elastic intermolecular interactions propagate the spin-state switching information throughout the lattice, the J–T distortion would act as a barrier and energetically separate the HS- and LS states of complex $[\text{Fe}(\text{BPP-COOEt})_2](\text{ClO}_4)_2 \cdot 1\text{CH}_3\text{CN}$, causing the formation of an ~ 101 K wide hysteresis loop. Based on the above discussion, we assume the J–T distorted nature of the HS-states of **1a–d** and **2** as a contributing factor in effecting the hysteretic spin-state switching associated with the complexes. The abruptness of the transition observed for **1a–b** and **2** could have arisen due to favourable intermolecular contacts propagating the spin-state switching throughout the crystal lattice. As a note to the reader, the above reductionist approach, attempting to rationalize SCO in complexes **1a–d** and **2**, needs to be considered with caution; other structural factors such as anion disorder, electrostatics, *etc.*, could have also contributed to the hysteretic SCO in the complexes.¹³

The situation is rather complicated for complex **1c**, which showed a lattice solvent-dependent SCO upon repeated heat-cool cycling. Such SCO is commonly observed for complexes crystallizing with lattice solvent molecules. Indeed, the high sensitivity of SCO to the presence or absence of lattice solvent molecules is a well-established phenomenon in the SCO research field. On the other hand, stepwise SCO is not a common occurrence in the case of mononuclear complexes such as $[\text{Fe}(\text{BPP-R})_2]^{2+}$ complexes; only a handful of $[\text{Fe}(\text{BPP-R})_2]^{2+}$ complexes have been reported showing stepwise SCO behaviour. It is interesting to note the step-like features present in the LS \rightarrow HS switching branches of **1c**. Although less pronounced, such features (shoulder-like) also appeared in the LS \rightarrow HS branches of **1a–b**. In all cases, the SCO became more gradual after the onset of the shoulder- or plateau-like features, effecting the formation of larger hysteresis widths relative to the ones observed for the abrupt SCO regions. Such observations point to the formation of a phase composed of specific proportions of LS and HS states—for example, 1 : 1 HS/LS observed at 241 K for **1a**. The nature of intermolecular interactions varies in the low- and high-temperature phases, causing the observed abrupt *versus* gradual SCO behaviour. The absence of such stepwise LS to HS switching in deliberately precipitated **1d** indicates the requirement of high-quality crystals with a singular arrangement, inducing shoulder-like SCO features. Besides, the more broadened reflections observed in the SWAXS patterns of **1d** relative to **1a** indicate different crystal sizes of the complexes with the size of **1d** in the nanometre range. Overall, the observed difference in the SCO between **1a** and **1d** could be attributed either to a specific crystalline arrangement or to the different sizes of the crystals. It is also possible that both factors contribute to the observed difference; an unambiguous elucidation requires further experimental investigations.

Conclusions

In conclusion, the pursuit of SCO complexes featuring a technologically relevant thermal hysteresis width ($\Delta T \geq 40$ K) centred at or around room temperature is still on. However, the bistable SCO characteristics associated with the complexes reported in this study are encouraging to pursue the study of the $[\text{Fe}(\text{BPP-R})_2]^{2+}$ family of complexes for the realization of technologically relevant SCO systems. The amenable nature of the $-\text{CN}$ group for further functional group transformation is ideally suited to design bistable $[\text{Fe}(\text{BPP-R})_2]^{2+}$ SCO complexes. For example, the conversion of the $-\text{CN}$ group to the tetrazole functional group could be used to construct an SCO-active lattice composed of hydrogen bond-forming self-assembling motifs. Moreover, deprotonation of the same tetrazole tethered BPP-ligand system under basic conditions could yield a mono-anionic ligand useful for the preparation of charge-neutral SCO complexes—such complexes are reported to undergo bistable SCO at or around room temperature.^{51,57} Moreover, the complexes reported in this study could be used to fabricate single molecule spin-state switchable junctions, taking advantage of the $-\text{CN}$ functionality as an anchoring group in molecular electronic junctions.⁵⁸

Experimental

Materials and methods

Anhydrous solvents, CuCN, $\text{Fe}(\text{BF}_4)_2 \cdot 6\text{H}_2\text{O}$, and $\text{Fe}(\text{ClO}_4)_2 \cdot 6\text{H}_2\text{O}$, were purchased from commercial sources and used as received. Glassware was dried in a vacuum oven at 150 °C prior to the experiments. Chemical reactions reported in this study were performed under an argon (Ar) atmosphere unless otherwise reported.

X-ray diffraction data collection was carried out on a Bruker APEX II DUO Kappa-CCD diffractometer equipped with an Oxford Cryo-system liquid N_2 device, using Cu-K α radiation ($\lambda = 1.54178$ Å). The crystal-detector distance was 40 mm. The cell parameters were determined using APEX2 software (M86-E01078 APEX2 User Manual, Bruker AXS Inc., Madison, USA, 2006) from reflections taken from three sets of 20 frames, each at 10 s exposure. The structure was solved by direct methods using the program SHELXS-2014.⁵⁹ The refinement and all further calculations were carried out using SHELXL-2014.⁶⁰ The H-atoms were included in calculated positions and treated as riding atoms using SHELXL default parameters. The non-H atoms were refined anisotropically, using weighted full-matrix least-squares on F^2 . A semi-empirical absorption correction was applied using SADABS in APEX2; transmission factors: $T_{\text{min}}/T_{\text{max}} = 0.5220/0.7528$.

Absorption spectra were measured on a Varian Cary 100 double-beam UV-VIS spectrophotometer and the baseline was corrected.

Magnetic measurements were performed on a MPMS-3 SQUID-VSM magnetometer (Quantum Design). The temperature dependent magnetization was recorded at an applied DC field of 0.1 T. Temperature sweeping rates of 5 K min^{-1} and 1 K min^{-1} were employed unless otherwise specified. Gelatine capsules were

used as sample holders in the 5 K to 300/400 K temperature range. The diamagnetic corrections of the molar magnetic susceptibilities were applied using Pascal's constants.

Differential scanning calorimetry (DSC) measurements were performed with a TA Instruments DSCQ1000 instrument operated at a scanning rate of 2 K min⁻¹. Small and wide angle X-ray scattering (SWAXS) patterns were obtained with a linear monochromatic Cu K_{α1} beam ($\lambda = 1.5405 \text{ \AA}$). The beam was obtained using a sealed-tube generator equipped with a bent quartz monochromator and a curved Inel CPS 120 counter gas filled detector. Periodicities up to 70 Å could be measured, and the sample temperature was controlled to within $\pm 0.01 \text{ }^\circ\text{C}$ from 20 °C to 200 °C. The sample was filled in Lindemann capillaries and exposure times were varied between 1 h and 24 h.

Synthesis of the ligand and complexes

Synthesis of 2,6-di(1H-pyrazol-1-yl)pyridine-4-carbonitrile (L). Copper(I)cyanide (0.323 g, $3.6 \times 10^{-3} \text{ M}$) was added to a solution of 4-iodo-2,6-di(1H-pyrazol-1-yl)pyridine (1 g, $\sim 3 \times 10^{-3} \text{ M}$) in 5 ml of dry DMF, and the reaction mixture was stirred at 130 °C for 12 h under argon protection. One gram of KCN dissolved in 10 mL of water was added to the cooled reaction mixture, and the mixture was stirred for 30 min and filtered. The filtrate was diluted with more water and extracted with DCM three times. The combined organic fractions were stored over Na₂SO₄ for 2 h. Column chromatography with silica gel and DCM as stationary and mobile phases, respectively, yielded the ligand as a white powder.

Yield: 0.5 g (71%). ¹H NMR (CDCl₃, 500 MHz): 8.56 (dd, $J = 2.68$ and 0.65), 8.10 (s), 7.84 (dd, $J = 1.59$ and 0.61) and 6.58 (dd, $J = 2.66$ and 1.64). ¹³C NMR (CDCl₃, 125 MHz): 150.8, 143.5, 127.3, 125.2, 115.9, 111.2, 109.1. ESI-MS: calculated for C₁₂H₉N₆ [M + H]⁺ = 237.09; found 237.09. Elemental analysis: calculated for C₁₂H₈N₆: C 61.01 H 3.41 N 35.58; found C 60.75 H 3.41 N 35.40.

Preparation of complexes 1a–c. To one eq. of ligand dissolved in 10 mL of dry acetonitrile, Fe(BF₄)₂·6H₂O (0.5 eq.) was added as a solid, and the mixture was swirled for a few seconds or until the occurrence of solubilization of the iron(II) salt. The reaction mixture was allowed to stand for a week, leading to the deposition of orange plate-like solids (1a), which were filtered off, washed with ether, and dried under vacuum overnight. The filtrate was portioned into test tubes and diethyl ether was allowed to slow-diffuse into the test tubes at 4 °C. This process resulted in the formation of orange plate-like (1b) and red-rod shaped (1c-ACN) crystals. The crystals were separated for analyses.

Elemental analysis of 1a: calculated for C₂₄H₁₆FeN₁₂B₂F₈: C, 41.07; H, 2.30; N, 23.95. Found: C, 41.14, H, 2.32, N, 23.78.

Elemental analysis of 1b: calculated for C₂₄H₁₆FeN₁₂B₂F₈: C, 41.07; H, 2.30; N, 23.95. Found: C, 41.10, H, 2.34, N, 23.70.

Elemental analysis of 1c: calculated for C₂₄H₁₆FeN₁₂B₂F₈·1CH₃CN: C, 42.03; H, 2.58; N, 24.51. Found: C, 41.33, H, 2.42, N, 24.02. The discrepancy between the calculated and obtained values is due to the loss of the lattice ACN solvent.

Elemental analysis of solvent-free 1c obtained after magnetic measurements: calculated for C₂₄H₁₆FeN₁₂B₂F₈: C, 41.07; H, 2.30; N, 23.95. Found: C, 40.8, H, 2.33, N, 23.75.

Complex 1d: to one eq. of ligand dissolved in 10 mL of dry acetonitrile and a dichloromethane (1 : 1 v/v) solvent mixture, Fe(BF₄)₂·6H₂O (0.5 eq.) was added as a solid, and the mixture was stirred for two hours, leading to the formation of a precipitate. The precipitate was filtered, washed with dichloromethane twice, and dried under vacuum to yield an orange-red powder (1d). Elemental analysis: calculated for C₂₄H₁₆FeN₁₂B₂F₈: C, 41.07; H, 2.30; N, 23.95. Found: C, 40.60, H, 2.32, N, 23.43.

Complex 2: to one eq. of ligand dissolved in 10 mL of dry acetonitrile, Fe(ClO₄)₂·6H₂O (0.5 eq.) was added as a solid, and an immediate precipitation occurred. The mixture was stirred for two hours, filtered, and the precipitate was washed with ether twice. Drying of the solids under vacuum yielded an orange powder (2). Elemental analysis: calculated for C₂₄H₁₆FeN₁₂Cl₂O₈: C, 39.64; H, 2.22; N, 23.11. Found: C, 39.43; H, 2.27; N, 22.62.

Caution! Perchlorate complexes are potential explosives and should be handled with care in small quantities. However, we experienced no problems while handling complex 2.

Conflicts of interest

There are no conflicts of interest to declare.

Acknowledgements

The authors thank Dr Guillaume Rogez, IPCMS, for the SQUID measurements. Grant Agency Innovation FRC is acknowledged for the financial support for the project Self-assembly of spin-crossover (SCO) complexes on graphene. M. R. thanks the DFG priority program 1928 "COORNETS" for generous support.

References

- 1 *Spin Crossover in Transition Metal Compounds I*, ed. P. Gütllich and H. A. Goodwin, Springer Berlin Heidelberg, Berlin, Heidelberg, 2004, vol. 233.
- 2 M. A. Halcrow, *Spin-crossover Materials: Properties and Applications*, Wiley, 2013.
- 3 K. Ridier, Y. Zhang, M. Piedrahita-Bello, C. M. Quintero, L. Salmon, G. Molnár, C. Bergaud and A. Bousseksou, *Adv. Mater.*, 2020, 2000987.
- 4 M. Palluel, N. M. Tran, N. Daro, S. Buffière, S. Mornet, E. Freysz and G. Chastanet, *Adv. Funct. Mater.*, 2020, **30**, 2000447.
- 5 E. P. Geest, K. Shakouri, W. Fu, V. Robert, V. Tudor, S. Bonnet and G. F. Schneider, *Adv. Mater.*, 2020, **32**, 1903575.
- 6 G. Molnár, M. Mikolasek, K. Ridier, A. Fahs, W. Nicolazzi and A. Bousseksou, *Ann. Phys.*, 2019, **531**, 1900076.

- 7 H.-Y. Sun, Y.-S. Meng and T. Liu, *Chem. Commun.*, 2019, **55**, 8359–8373.
- 8 S. Decurtins, P. Gütllich, C. P. Köhler, H. Spiering and A. Hauser, *Chem. Phys. Lett.*, 1984, **105**, 1–4.
- 9 A. Hauser, *Comments Inorg. Chem.*, 1995, **17**, 17–40.
- 10 J.-F. Létard, P. Guionneau and L. Goux-Capes, *Spin Crossover in Transition Metal Compounds III*, Springer-Verlag, Berlin/Heidelberg, 2004, vol. 235, pp. 221–249.
- 11 A. Bousseksou, G. Molnár, L. Salmon and W. Nicolazzi, *Chem. Soc. Rev.*, 2011, **40**, 3313.
- 12 E. Collet and P. Guionneau, *C. R. Chim.*, 2018, **21**, 1133–1151.
- 13 M. A. Halcrow, *Chem. Soc. Rev.*, 2011, **40**, 4119.
- 14 G. J. Halder, *Science*, 2002, **298**, 1762–1765.
- 15 R. W. Hogue, S. Singh and S. Brooker, *Chem. Soc. Rev.*, 2018, **47**, 7303–7338.
- 16 O. Kahn, *Curr. Opin. Solid State Mater. Sci.*, 1996, **1**, 547–554.
- 17 M. Ruben, J. Rojo, F. J. Romero-Salguero, L. H. Uppadine and J.-M. Lehn, *Angew. Chem., Int. Ed.*, 2004, **43**, 3644–3662.
- 18 J. Tao, R.-J. Wei, R.-B. Huang and L.-S. Zheng, *Chem. Soc. Rev.*, 2012, **41**, 703–737.
- 19 P. Guionneau, *Dalton Trans.*, 2014, **43**, 382–393.
- 20 S. Venkataramani, U. Jana, M. Dommaschk, F. D. Sonnichsen, F. Tuzcek and R. Herges, *Science*, 2011, **331**, 445–448.
- 21 M. A. Halcrow, *Dalton Trans.*, 2020, DOI: 10.1039/D0DT01919D.
- 22 M. A. Halcrow, *Chem. Lett.*, 2014, **43**, 1178–1188.
- 23 O. Kahn, J. Kröber and C. Jay, *Adv. Mater.*, 1992, **4**, 718–728.
- 24 M. Ruben and K. S. Kumar, *Angew. Chem., Int. Ed.*, 2019, DOI: 10.1002/anie.201911256.
- 25 K. Senthil Kumar and M. Ruben, *Coord. Chem. Rev.*, 2017, **346**, 176–205.
- 26 A. Köbke, F. Gutzeit, F. Röhrich, A. Schlimm, J. Grunwald, F. Tuzcek, M. Studniarek, D. Longo, F. Choueikani, E. Otero, P. Ohresser, S. Rohlf, S. Johannsen, F. Diekmann, K. Rosnagel, A. Weismann, T. Jasper-Toennies, C. Näther, R. Herges, R. Berndt and M. Gruber, *Nat. Nanotechnol.*, 2020, **15**, 18–21.
- 27 K. P. Kepp, *Coord. Chem. Rev.*, 2017, **344**, 363–374.
- 28 Z. Wu, *J. Geophys. Res.: Solid Earth*, 2016, **121**, 2304–2314.
- 29 T. Miyamachi, M. Gruber, V. Davesne, M. Bowen, S. Boukari, L. Joly, F. Scheurer, G. Rogez, T. K. Yamada, P. Ohresser, E. Beaurepaire and W. Wulfhekel, *Nat. Commun.*, 2012, **3**, 938.
- 30 B. Weber, W. Bauer and J. Obel, *Angew. Chem., Int. Ed.*, 2008, **47**, 10098–10101.
- 31 B. Schäfer, C. Rajnák, I. Šalitroš, O. Fuhr, D. Klar, C. Schmitz-Antoniak, E. Weschke, H. Wende and M. Ruben, *Chem. Commun.*, 2013, **49**, 10986.
- 32 H. Hagiwara, T. Masuda, T. Ohno, M. Suzuki, T. Udagawa and K. Murai, *Cryst. Growth Des.*, 2017, **17**, 6006–6019.
- 33 C. Lochenie, K. Schötz, F. Panzer, H. Kurz, B. Maier, F. Puchtler, S. Agarwal, A. Köhler and B. Weber, *J. Am. Chem. Soc.*, 2018, **140**, 700–709.
- 34 J. M. Holland, C. A. Kilner, M. Thornton-Pett, M. A. Halcrow, J. A. McAllister and Z. Lu, *Chem. Commun.*, 2001, 577–578.
- 35 L. J. Kershaw Cook, R. Kulmaczewski, R. Mohammed, S. Dudley, S. A. Barrett, M. A. Little, R. J. Deeth and M. A. Halcrow, *Angew. Chem., Int. Ed.*, 2016, **55**, 4327–4331.
- 36 L. J. Kershaw Cook, R. Mohammed, G. Sherborne, T. D. Roberts, S. Alvarez and M. A. Halcrow, *Coord. Chem. Rev.*, 2015, **289–290**, 2–12.
- 37 M. A. Halcrow, *New J. Chem.*, 2014, **38**, 1868–1882.
- 38 M. A. Halcrow, *Coord. Chem. Rev.*, 2009, **253**, 2493–2514.
- 39 M. A. Halcrow, *Coord. Chem. Rev.*, 2005, **249**, 2880–2908.
- 40 M. Halcrow, *Crystals*, 2016, **6**, 58.
- 41 K. Senthil Kumar, B. Heinrich, S. Vela, E. Moreno-Pineda, C. Bailly and M. Ruben, *Dalton Trans.*, 2019, **48**, 3825–3830.
- 42 *Comprehensive Organic Name Reactions and Reagents*, ed. Z. Wang, John Wiley & Sons, Inc., Hoboken, NJ, USA, 2010.
- 43 R. Pritchard, C. A. Kilner and M. A. Halcrow, *Chem. Commun.*, 2007, 577–579.
- 44 L. J. Kershaw Cook, R. Kulmaczewski, S. A. Barrett and M. A. Halcrow, *Inorg. Chem. Front.*, 2015, **2**, 662–670.
- 45 M. Seredyuk, M. C. Muñoz, M. Castro, T. Romero-Morcillo, A. B. Gaspar and J. A. Real, *Chem. – Eur. J.*, 2013, **19**, 6591–6596.
- 46 M. Weselski, M. Książek, D. Rokosz, A. Dreczko, J. Kusz and R. Bronisz, *Chem. Commun.*, 2018, **54**, 3895–3898.
- 47 M. Weselski, M. Książek, P. Mess, J. Kusz and R. Bronisz, *Chem. Commun.*, 2019, **55**, 7033–7036.
- 48 R. G. Miller and S. Brooker, *Chem. Sci.*, 2016, **7**, 2501–2505.
- 49 M. Fumanal, F. Jiménez-Grávalos, J. Ribas-Arino and S. Vela, *Inorg. Chem.*, 2017, **56**, 4474–4483.
- 50 R. Kulmaczewski, E. Trzop, E. Collet, S. Vela and M. A. Halcrow, *J. Mater. Chem. C*, 2020, **8**, 8420–8429.
- 51 K. Senthil Kumar, S. Vela, B. Heinrich, N. Suryadevara, L. Karmazin, C. Bailly and M. Ruben, *Dalton Trans.*, 2020, **49**, 1022–1031.
- 52 L. J. Kershaw Cook, F. L. Thorp-Greenwood, T. P. Comyn, O. Cespedes, G. Chastanet and M. A. Halcrow, *Inorg. Chem.*, 2015, **54**, 6319–6330.
- 53 M. Sorai, Y. Nakazawa, M. Nakano and Y. Miyazaki, *Chem. Rev.*, 2013, **113**, PR41–PR122.
- 54 W. Nicolazzi and A. Bousseksou, *C. R. Chim.*, 2018, **21**, 1060–1074.
- 55 A. Bousseksou, J. J. McGarvey, F. Varret, J. A. Real, J.-P. Tuchagues, A. C. Dennis and M. L. Boillot, *Chem. Phys. Lett.*, 2000, **318**, 409–416.
- 56 H. Douib, L. Cornet, J. F. Gonzalez, E. Trzop, V. Dorcet, A. Gouasmia, L. Ouahab, O. Cadour and F. Pointillart, *Eur. J. Inorg. Chem.*, 2018, **2018**, 4452–4457.
- 57 K. Senthil Kumar, I. Šalitroš, B. Heinrich, O. Fuhr and M. Ruben, *J. Mater. Chem. C*, 2015, **3**, 11635–11644.
- 58 T. A. Su, M. Neupane, M. L. Steigerwald, L. Venkataraman and C. Nuckolls, *Nat. Rev. Mater.*, 2016, **1**, 16002.
- 59 G. M. Sheldrick, *Acta Crystallogr., Sect. A: Found. Adv.*, 2015, **71**, 3–8.
- 60 G. M. Sheldrick, *Acta Crystallogr., Sect. C: Struct. Chem.*, 2015, **71**, 3–8.